NOTICE CONCERNING COPYRIGHT RESTRICTIONS

Surface Deformation at the San Emidio Geothermal Field, Nevada, from Satellite Radar Interferometry

**Mariana Eneva[1], Giacomo Falorni[2], William Teplow[3],
Jessica Morgan[2], Greg Rhodes[4], and David Adams[1]**

[1]Imageair, Inc.
[2]TRE Canada Inc.
[3]US Geothermal Inc.
[4]Department of Geological Sciences and Engineering, University of Nevada Reno

Keywords

Satellite radar interferometry, InSAR, SqueeSAR, surface deformation, San Emidio, geothermal

ABSTRACT

As part of a DOE project, we have applied satellite radar interferometry (InSAR) to detect surface deformation in the San Emidio geothermal field, Nevada. The specific method used, SqueeSAR™, is the latest innovation in the field of InSAR, which allows obtaining deformation time series at locations of permanent and distributed scatterers (PS and DS, respectively). The PS points are relatively small objects such as buildings, wellheads, boulders, etc., which remain coherent from one satellite scene to another. The DS are coherent areas covering several pixels emitting weaker signals than the PS, but still have acceptable signal-to-noise ratios. The PS and DS play the role of numerous benchmarks, at which surface deformation rates can be determined.

Three sets of radar data were used covering an area of 60 km². The datasets included imagery from the European ERS-1, ERS-2, and Envisat satellites. They consisted of 38 ERS-1/2 scenes acquired from descending orbits (satellite moving north to south) during the period May 1992 – January 2001, 53 descending Envisat images collected between June 2004 and April 2010, and 45 ascending (satellite moving south to north) Envisat scenes from the period October 2003 – June 2010. Due to the desert environment of the study area, numerous PS and DS were identified - more than 180,000 from the ERS descending, 212,000 from the Envisat descending, and 166,000 from the Envisat ascending scenes. Surface deformation at the individual PS and DS locations is first determined in the line-of-sight (LOS)

direction to the satellite; i.e., in terms of movement towards or away from it. The availability of Envisat data from two orbit geometries (descending and ascending) makes it possible to decompose the LOS deformation into vertical displacements and movements in the west-east horizontal direction. Due to the steep look angle of the satellites (~21º to 22º), the vertical and the LOS movements are very similar. However, the west-east horizontal component of deformation is only revealed by the decomposition procedure.

The LOS time series were used to derive surface deformation rates at all individual PS and DS locations, while vertical and west-east horizontal rates were extracted from the combinations of descending and ascending LOS rates. Distinct areas of subsidence and uplift are outlined, with changing spatial patterns in time, especially from the older ERS data set to the newer Envisat data. We observe surface deformation
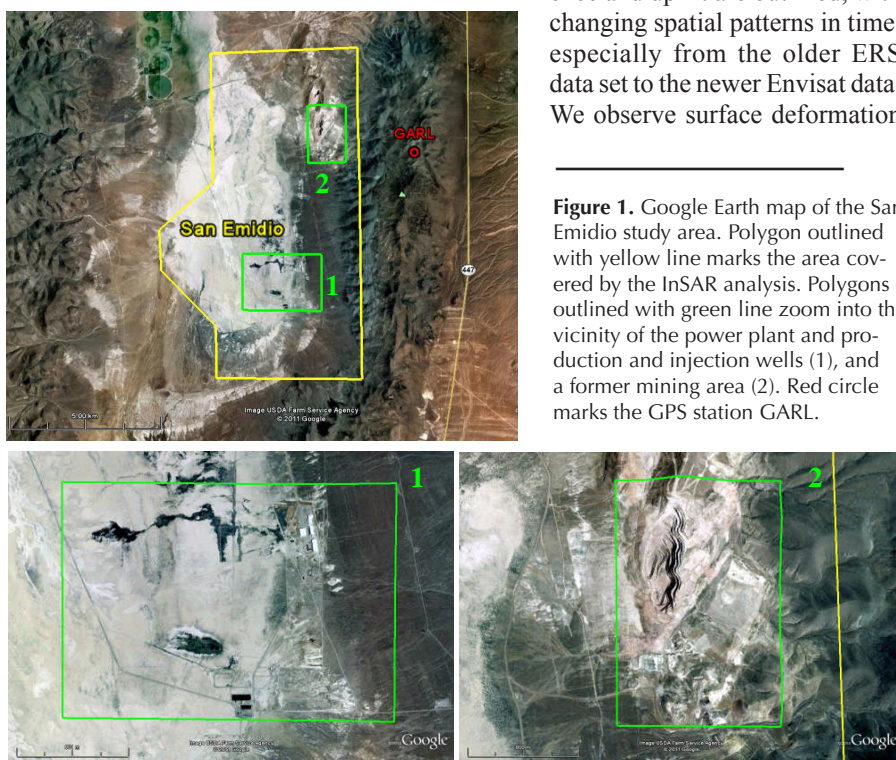
Figure 1. Google Earth map of the San Emidio study area. Polygon outlined with yellow line marks the area covered by the InSAR analysis. Polygons outlined with green line zoom into the vicinity of the power plant and production and injection wells (1), and a former mining area (2). Red circle marks the GPS station GARL.

in the area of the production wells, and profiles transecting faults indicate distinct signals, likely resulting from hydrological control. Many of the deformation time series exhibit obvious seasonal patterns, with varying amplitudes throughout the study area. We continue to examine these uniquely rich results for clues to describe the geothermal resource at San Emidio.

Introduction

The study area including the San Emidio geothermal field is shown in Figure 1. It is located in the eastern part of the San Emidio Desert and covers ~60 km^2. The geothermal potential of the area was not known until the 1960's, when hot water was encountered in shallow exploration drill holes. Temperatures encountered were 53^{0}C at 1-m depth, boiling water at 29.5 m, and up to 127^{0}C at two Chevron Oil Co. test wells at depths 1,223 m and 1636 m. A binary geothermal power plant has been operating within the study area since 1987. It is currently producing 2.3 MW electricity from a 155^{0}C resource. The insets in Fig. 1 show the area including the power plant, and the injection and production wells (Area 1), as well as a former mining area (Area 2).

The San Emidio Desert is an east-tilted half graben. Structural controls of the area have been studied by Moore (1979), Wood (1990), and Rhodes et al. (2010). The eastern San Emidio Desert and the adjacent Lake Range are characterized by a mainly N-striking, W-dipping normal fault pattern (Figure 2a). There are two important exceptions to this pattern. One is a NNE-striking normal fault which intersects the San Emidio fault in an area of high fault density near the currently operating geothermal plant and production wells. The second is an ENE-striking, sinistral-normal, oblique-slip fault which functions as a hard-linking step-over between two strands of the main N-striking, W-dipping range-front fault. Abundant hydrothermal alteration and silicification are observed at this step-over. The main range-front, the Northern Lake Range fault, has approximately 2 km of normal offset. The San Emidio fault is a hydrothermally altered Holocene fault scarp spatially related to the geothermal production zone and a shallow thermal anomaly. This fault is characterized by approximately 175 m of normal offset. The GPS station GARL (Fig. 1) west of the study area indicates subsidence of ~0.9 mm/year, southward movement of ~7.7 mm/year and westward movement of ~17.2 mm/year (from http://sopac/ucsd.edu).

In 2009 U.S. Geothermal Inc., which leases the San Emidio resource area, proposed to develop an exploration strategy and a suite of innovative geophysical techniques for the purpose of precisely locating large aperture fractures distributed within the faulted and fractured geothermal system. The resulting DOE cost-shared project combined InSAR for detection of surface deformation, structural analysis and a seismic survey. The area within the southern exploration block containing known large-aperture fracture zones encountered in four wells was used as control to judge the efficacy of the methods employed (Fig. 2a).

Satellite radar interferometry, or interferometric aperture radar (InSAR), has found numerous applications over the last several decades. In particular, the traditional differential InSAR (DInSAR) method has been used to detect subsidence from a variety of causes, such as earthquakes, water pumping, mining (e.g., Eneva, 2010), etc. There have also been observations at geothermal

fields (e.g., Oppliger et al., 2008; Wicks et al., 2001). A recent innovation, PSInSAR^{TM} (Ferretti et al., 2000, 2007) makes use of so-called "permanent scatterers" (PS), to produce detailed deformation time series and deformation rates. PS are objects, such as buildings, fences, lampposts, transmission towers, rock outcrops, etc., which serve as reflectors of the radar microwaves. We have previously used the PSInSAR^{TM} method to detect subsidence at the Salton Sea geothermal field (Eneva et al., 2009; Eneva and Adams, 2010; Falorni et al., 2011). The latest innovation of this method is SqueeSAR^{TM} (Ferretti et al., 2011), which adds to the PS locations also "distributed scatterers" (DS). DS are homogeneous areas emitting signals with smaller signal-to-noise ratios than the PS, but still significantly above the background. These include rangelands, pastures, and bare earth characteristic of arid environments. Falorni et al. (2011) discuss the potential of PSInSAR^{TM} and SqueeSAR^{TM} for geothermal applications.

Hereafter, "InSAR results" and "InSAR analysis" specifically refer to the SqueeSAR^{TM} procedure applied to the satellite data collected over the San Emidio study area.

Methodology and Datasets

The SqueeSAR^{TM} method was applied to three data sets collected over the San Emidio area: 38 descending images from the ERS-1 and ERS-2 satellites for the period 05/03/1992 – 01/10/2001; 53 descending images from the Envisat satellite for the period 06/23/2004 – 04/28/2010; and 45 ascending images from Envisat for the period 10/29/2003 – 06/09/2010. Descending and ascending scenes are those collected while the satellites orbited north to south or south to north, respectively. All three datasets contained a sufficient number of images to meet the minimum of 15 scenes required to apply the SqueeSAR^{TM} technique. The deformation is first obtained in the line-of-sight (LOS) direction. It is considered negative when the movement is away from the satellite and positive towards the satellite. Because of the steep viewing angle from the satellite, the LOS deformation is rather close to the vertical movement. Hence, movement away from the satellite is mostly representative of subsidence, and towards the satellite, of uplift. However, when data are available from both descending and ascending orbits, it is also possible to decompose the LOS deformation into vertical and horizontal components. Although only the west-east component of the horizontal displacement is captured, this represents a significant advantage. In this case, negative values indicate westward movement and positive values indicate eastward movement. The deformation time series are fitted with straight lines and their slopes are used to estimate the deformation rates. These results are featured in subsequent figures.

Displacement measurements in any InSAR studies are done relative to a reference point, considered to be motionless. The method thus measures local movements and does not show regional movements affecting the entire study area and its vicinity. Ideally, the movements at the reference point would be known. However, in this study, the closest GPS station GARL (Fig. 1) is too far away to be used as a reference point. Therefore, local reference points were chosen around the middle of the eastern part of the study area. Because these points depend on the specific data used, they are somewhat different for the three data sets – 2 m apart between the Envisat descending and ascending data sets,

and 500 m between the Envisat and ERS data sets. For all practical purposes, we consider these locations close enough to be able to compare results from the three data sets. The reference points are shown in Figs. 2b-2d.

We have created codes and animations, which allow us to examine various aspects of the results. There are numerous factors to consider and the work is still ongoing. For example, it is possible to study individual polygons of arbitrary size, and to examine individual and mean time series from the PS and DS in them, as well as the degree of linearity of the time series. We also study profiles, displaying both the deformation rates and cumulative deformation along them.

Results and Discussion

Because the desert environment of the San Emidio study area is devoid of vegetation, numerous PS and DS locations were identi-
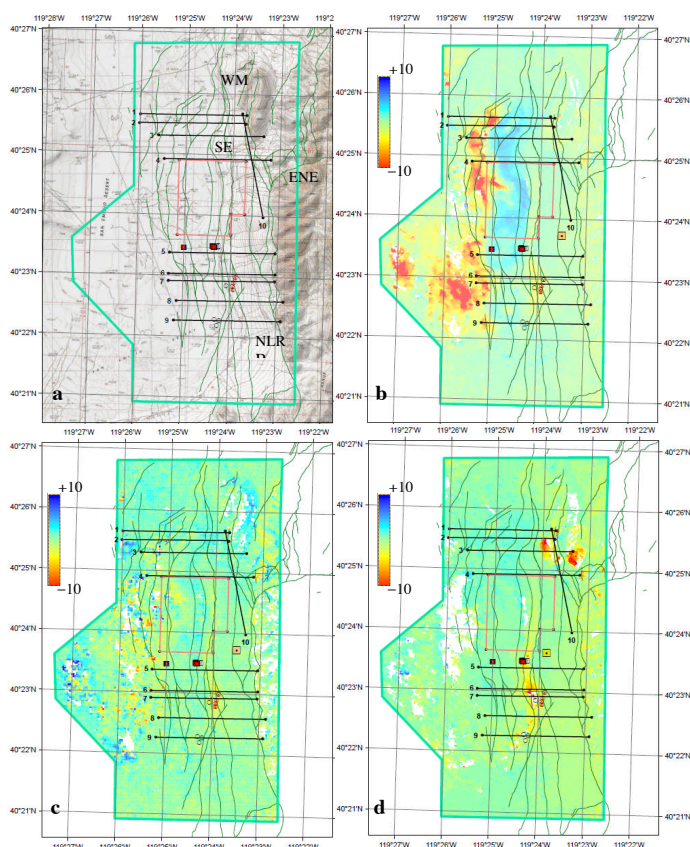
Figure 2. Maps showing InSAR results. Numbered black lines show 10 seismic lines. Polygon outlined with red marks inaccessible private property. Circles mark injection and production wells, squares mark Chevron wells. Red crosses denote wells where fracturing was observed. Dark green lines mark faults. (a) Topographic map. Marked faults are San Emidio (SE), North Lake Range (NLR), East North East (ENE), and Wind Mountain (WM). (b) LOS deformation from Envisat data. (c) West-east component of deformation from Envisat data in 50-m cells. (d) LOS deformation from ERS data. The color scale shows surface deformation in mm/year. Yellow to red colors indicate displacements away from the satellite in (b) and (d), which are also representative of subsidence, and westward horizontal movements in (c). Green to blue colors indicate movements in the opposite direction. In (b)-(d) yellow squares with dots inside, located around the middle eastern part of the study area, mark the reference points used to measure the surface deformation.

fied - more than 180,000 from the ERS descending, 212,000 from the Envisat descending, and 166,000 from the Envisat ascending scenes. Of these, the PS locations were 3459, 28471 and 21171, respectively. Deformation time series were obtained for each of the PS and DS and were subsequently used to extract deformation rates.

Map displays of the deformation rates reveal informative patterns, which can be explained with the effects of several factors. Figure 2 shows map results from the InSAR analysis of the three data sets, along with mapped faults and ten seismic lines executed as part of the overall study. Also shown are three injection wells in the southernmost part of the study area close to the power plant, five production wells north-east of the injection wells, and two test wells drilled by Chevron Oil Co. in 1978. The color coded panels in Fig. 2 show annual deformation rates in mm/year, with "warm" colors (yellow to red) indicating negative values and "cold" colors (green to blue) marking positive values. Negative values indicate movements away from the satellite where LOS displacements are shown (Fig. 2b, 2d). For decomposed movements, negative values indicate subsidence or westward horizontal movement (Fig. 2c). Positive values indicate movements in the opposite direction - towards the satellite, or uplift, or eastward horizontal movement. Areas where movements could not be resolved by InSAR analysis are left white.

Fig. 2b shows the LOS deformation rates extracted from the Envisat descending images. The LOS deformation from the Envisat ascending images and the vertical deformation calculated after decomposition of the two sets of LOS deformation rates (Envisat descending and ascending) look very similar to Fig. 2b and are not shown here. While Fig. 2b is fairly representative of the vertical rates, information on horizontal movements can only be obtained through decomposition, and its pattern is quite different from that seen in Fig. 2b. The west-east horizontal component (Fig. 2c) does not reach the large values of vertical deformation observed in the western part of the study area. However, vertical and horizontal rates can be quite comparable elsewhere, as shown in some of the subsequent figures. Fig. 2d shows the LOS deformation rates from the ERS data.

Both Fig. 2b (Envisat LOS) and Fig. 2d (ERS LOS) indicate subsidence around the production wells. However, there are obvious differences between the two panels. The ERS rates (Fig. 2d) show high levels of subsidence in the north-eastern part of the area due to mining that took place within that period of time (1992-2000). It did not continue in the later Envisat period of time (2003-2010), so subsidence in the mining area is almost absent in Fig. 2b. Another significant difference between ERS and Envisat LOS rates is found in the western part of the study area. Here maximum subsidence values are seen in Fig. 2b (Envisat data), whereas much lower values are seen in Fig. 2d (ERS data), even though the InSAR analysis did not resolve the movements everywhere. These differences are most likely due to climatic changes, especially precipitation, as shown below.

Zooming in on Fig. 2 makes the individual PS and DS locations visible. The panels in Figure 3, derived from Figs. 2b and 2d, are expanded views of the mining area and the area surrounding the production wells. The PS and DS locations are color-coded depending on the rates extracted from the deformation time series. Other than the greatly diminished subsidence in the mining area
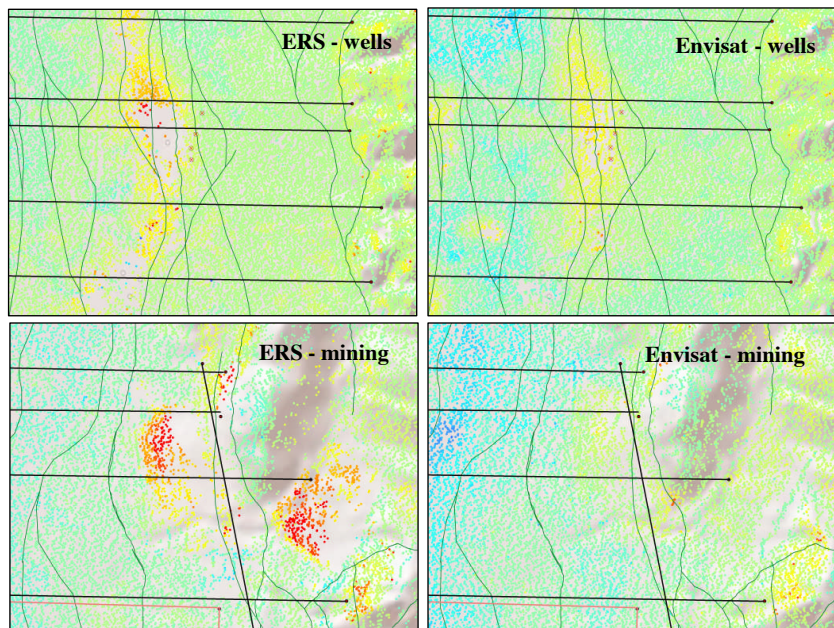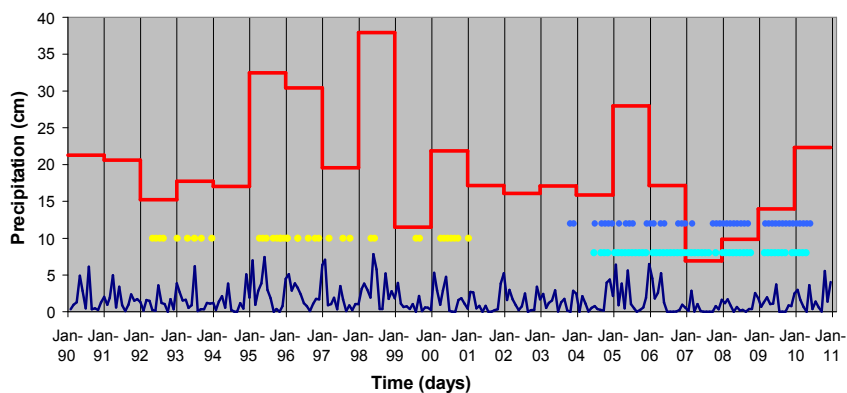
Figure 3. InSAR results in the vicinity of the injection and production wells (top), and the mining area (bottom). Left – zoom in Fig. 2d (ERS descending LOS rates). Right – zoom in Fig. 2b (Envisat descending LOS rates). Notations like in Fig. 2. Maps superimposed on shaded relief from DEM.

Figure 4. Precipitation at weather station Gerlach, Nevada. Dark blue line shows monthly precipitation levels. Red line shows yearly precipitation. Circles mark the time of the images used in the InSAR analysis from ERS descending (yellow), Envisat descending (light blue), and Envisat ascending (darker blue). Precipitation data from http://www.wrcc.dri.edu.
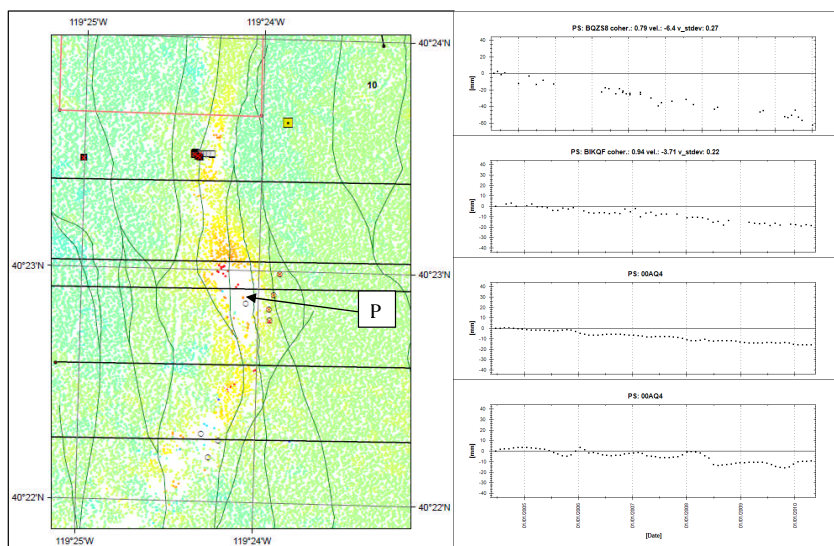

in 2003-2010 compared with 1992-2000, the increased detail shows clearly that the subsidence rates in the area around the production wells were in some parts larger in the earlier, ERS period. Deformation was not resolved from the ERS data in a significant part of this area (where PS and DS are absent). This may be a result of a higher gradient of subsidence, which could not be captured with this analysis, or due to the inferior quality of the ERS imagery compared to that from Envisat.

The relatively large subsidence signal in the western part of the study area and uplift just east of it (Fig. 2) are most likely related to the response of the sediments to variations in precipitation and temperature. This pattern illustrates the multiple causes of surface deformation that have to be taken into account. It is notable that the pattern is significantly stronger in the 2003-2010 period. To look for clues why this is so, we searched for weather stations in the vicinity of the study area. The closest station in this desert environment is Gerlach, Nevada, for which precipitation data were downloaded from the Western Regional Climate Center of the Desert Research Institute in Reno, Nevada. This station is 26 km north of the GPS station GARL, so it falls outside the map shown in Fig.1. Figure 4 shows the monthly precipitation rates, as well as the total annual rates. The driest months of the year are generally July and August, and they are drier in some years than others. The precipitation during the period covered by the Envisat data (2003-2010) was about 30% lower than that during the ERS period (1992-2000). This may explain the enhanced subsidence patterns seen in the western part of the study area in the later period covered by Envisat.

The deformation rates shown in color in Figs. 2 and 3 are extracted as slopes of the straight lines fitted to the time series in the individual PS and DS locations. Figure 5 shows examples of the time series at one particular PS location, which is near one of the production wells. The map in the figure shows only the ERS LOS deformation, which corresponds to the example of a time series given in the top panel on the left. The time series indicates an overall linear pattern of movement away from the satellite. The annual rate (i.e., the slope

Figure 5. Example of deformation time series at a PS point (P) near one of the production wells. Left – zoom in the southern part of Fig. 2d, showing color coded ERS LOS deformation rate in mm/year (color bar like in Fig. 2). Right – from top to bottom, time series show surface deformation (in mm) at P as follows: ERS LOS, Envisat LOS, Envisat 50-m vertical, and Envisat 50-m horizontal west-east movements.
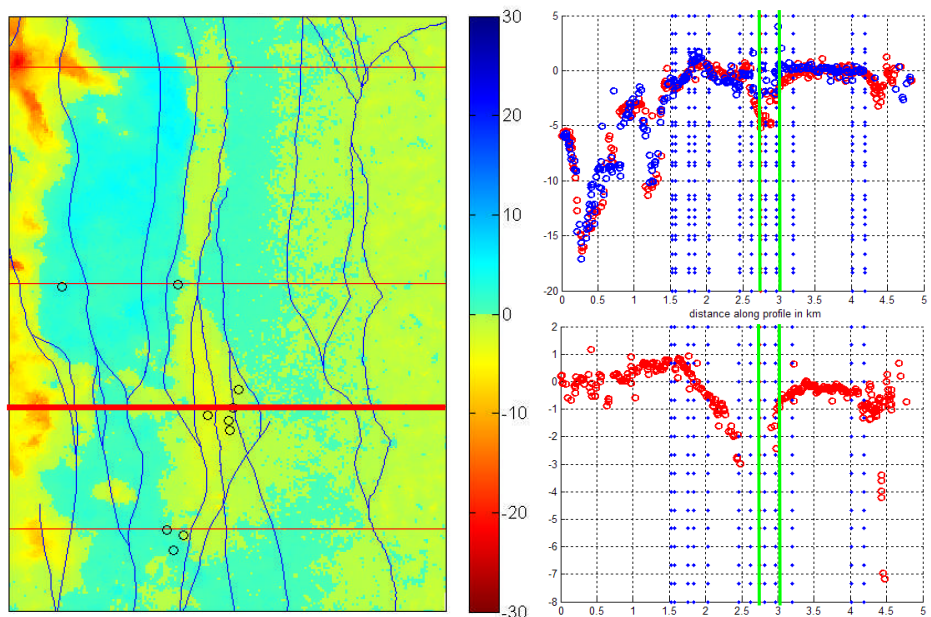
Figure 6. Example of LOS deformation rates along a profile. Left – map of LOS deformation rates in mm/year from Envisat descending data. Red horizontal lines show various studied profiles. Thick red line shows profile featured on the right. Other notations like in Fig. 2. Right – Plots of LOS deformation rates in mm/year along profile. Vertical dark blue dotted lines mark the locations where the profile crosses faults. Vertical green lines show production wells within 50 m of profile. Top plot shows LOS deformation rates from Envisat with circles – descending in red and ascending in blue. Bottom plot shows LOS deformation rate from ERS.
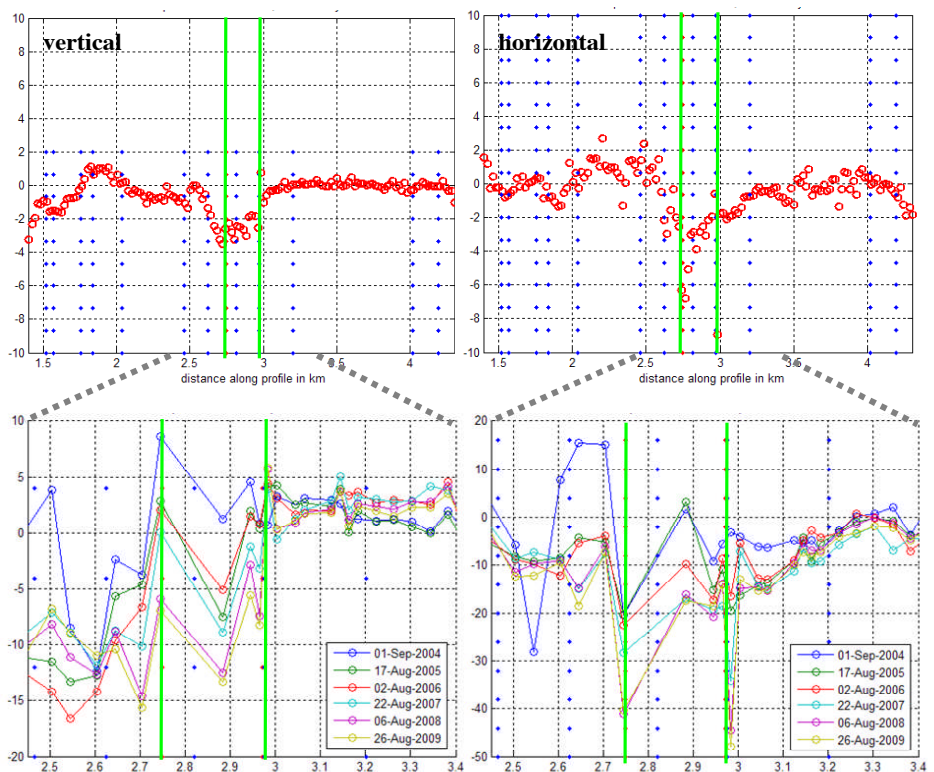
Figure 7. Plots of Envisat vertical (left panels) and west-east horizontal (right panels) deformation along a portion of the profile from Fig. 6. Top – deformation rates in mm/year. Bottom – zoom in a smaller portion of the profile. Cumulative deformation in mm from the summers of 2004-2009, color-coded as shown in legend. Other notations like in Fig. 6.

of the linear trend fitted to the time series) is −6.4 mm/year. The second panel shows the time series at that same location, but from the Envisat LOS deformation (map not shown) from the descending images. This time series indicates a slower rate, −3.4 mm/year. Using the Envisat ascending results for the LOS deformation (not shown), a decomposition is performed, which results in vertical and west-east components of the deformation time series at this location. The vertical time series indicates a very similar rate to that from the LOS deformation, as would be expected due to the steep look angle of Envisat. It shows downward movement, i.e., subsidence. The west-east component of the horizontal movement, shown in the bottom panel on the right, indicates negative values of the time series, i.e., westward movement.

Displaying the deformation rates along profiles of interest can be very informative. Figure 6 compares the LOS deformation rates from ERS and Envisat along a profile, which passes in the vicinity of two production wells and crosses 12 surface fault traces. For Envisat there are two types of LOS deformation series, calculated from the descending and ascending images. The dip around the production wells is clearly indicated in all datasets, even though the ERS observations have a gap where InSAR could not resolve the deformation. The Envisat data show the largest subsidence along the western part of this profile, which was already attributed to the drier years covered by the Envisat data (2003-2010).

Zooming in on the deformation rate plots in Fig. 6, Figure 7 shows parts of the same profile, where the LOS deformation data from the Envisat descending and ascending scenes were used to obtain the vertical and west-east horizontal rates. The top plots show subsidence around the production wells accompanied by westward horizontal movements. Both rates reach −4 mm/year, with the horizontal rates jumping to double that at some locations of the profile.

The bottom panels of Fig. 7 zoom in on yet a smaller portion of the profile and instead of showing the rates estimated over the whole time series, show the progression of deformation with time, i.e. the cumulative surface displacement. To avoid periodic influence of the seasonal changes, only deformation at late summer is shown, at six times about one year apart. Even though these time series appear rather noisy, following the color-coded cumulative deformation along the profile
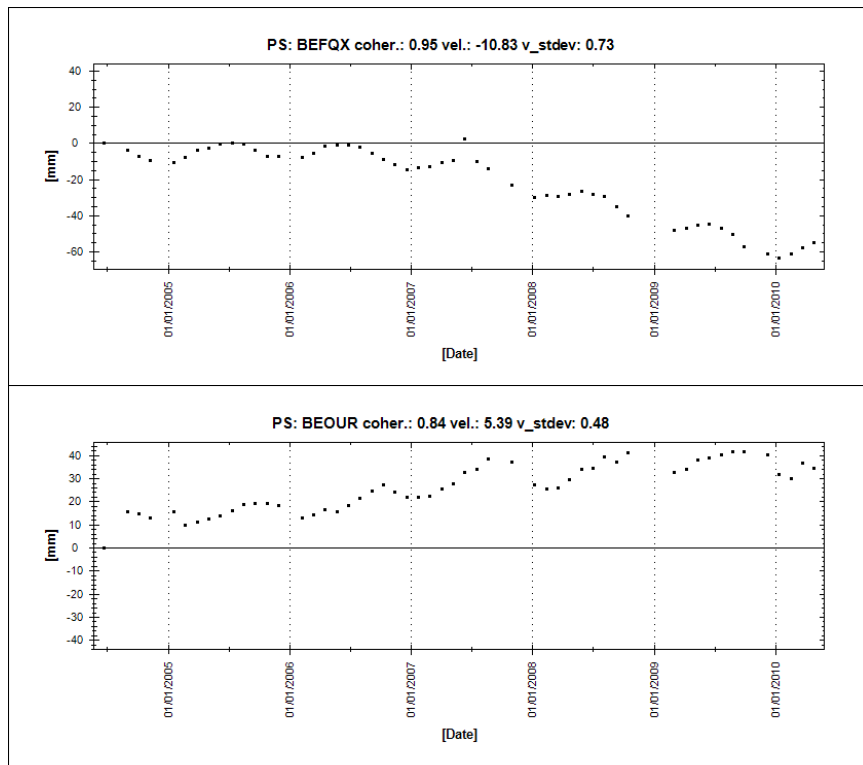
Figure 8. Example of time series showing seasonal variations. Top – subsidence. Bottom – uplift.
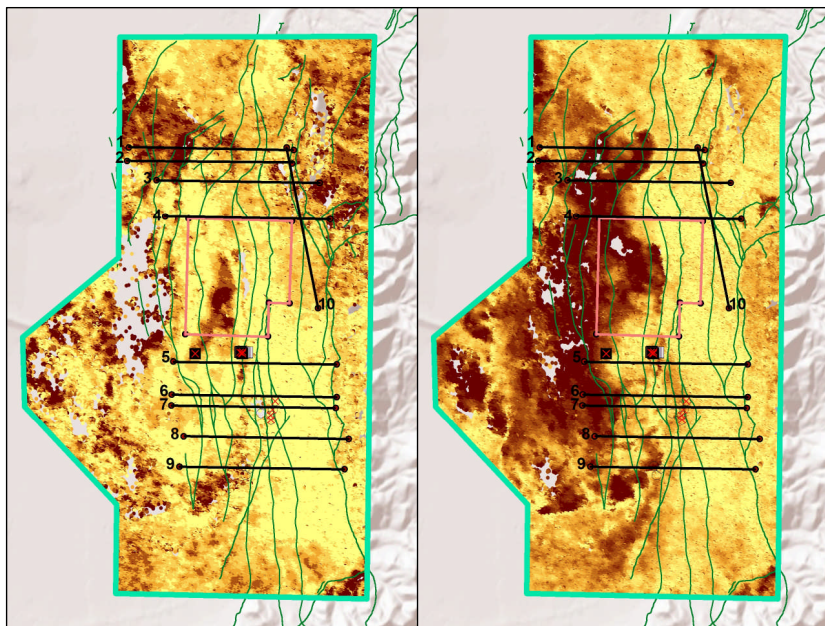
Figure 9. Map of seasonal amplitudes of time series. Values increase from yellow to brown. Left – ERS descending. Right – Envisat descending.

clearly indicates successive development of both subsidence and westward deformation around the two production wells.

As mentioned above, deformation exhibits seasonal changes. Figure 8 shows two examples at different PS locations, with time series indicating subsidence and uplift. In both cases the periodic seasonal changes are quite pronounced. Although many time series

exhibit such seasonal changes, the effect is not equally strong throughout the area. Figure 9 shows maps of seasonal amplitudes based on the ERS and Envisat results. The effect is more pronounced in the western part of the study area in the Envisat period, pointing for the most part to the areas exhibiting the greatest subsidence during the relative drought of that period (Fig. 2b). The area of the production wells apparently exhibits seasonal effects as well, although at a lower level. This illustrates once again that distinguishing between the various reasons for surface deformation is not straightforward.

Shallow injection has been ongoing throughout the periods covered by both the ERS and Envisat datasets and may have a significant impact on inflation patterns within the study area. During the six years of Envisat data, 4.8×10^7 cubic meters of geothermal fluid have been injected into the shallow aquifer at a depth of 70 to 100 m. If this injectate were confined to the area of inflation bounded by the San Emidio Fault to the east and the area of maximum subsidence to the west, it would cover approximately 7 km^2. During the six year period covered by Envisat data, this would represent a water depth of 6.9 m over the entire inflation area. Hence, injection must be considered a significant factor in understanding the surface deformation throughout the study area.

Another significant observation is that surface deformation sometimes shows distinct signals along profiles transecting faults. If deformation were purely tectonic, subsidence would be expected west of the surface traces of the faults in the study area, as they are mostly normal and dipping to the west. A subsidence pattern can logically be associated with interplay of eastward and westward horizontal movements on the flanks. Figure 10 shows an example of a profile crossing a single surface trace of a fault, which is away from either production, or areas of strong drought and seasonal effects. It is evident that the trace of the fault is associated with sharp jumps in the vertical and horizontal movements. In this example, the subsidence west of the fault reaches −5 mm/year, while the westward movement reaches +8 mm/year. Obviously, if all faults in the area show such amounts of movement, it cannot be only due to tectonic factors, because the cumulative tectonic effect would be unrealistically large. However, many faults show distinct signals in the opposite direction of what is tectonically expected. This leads us to the conclusion that the main control of surface deformation is likely of hydrological origin, both from climatic changes and underground water. Nonetheless, the observation of distinct signals marking the locations of faults is very significant, even if it is not clear how to deduce the tectonic movements on these faults from the InSAR results.

Other effects, which can be discerned from the InSAR deformation rates, appear associated with topography and possibly organized creep down slope, visible in the easternmost part of the
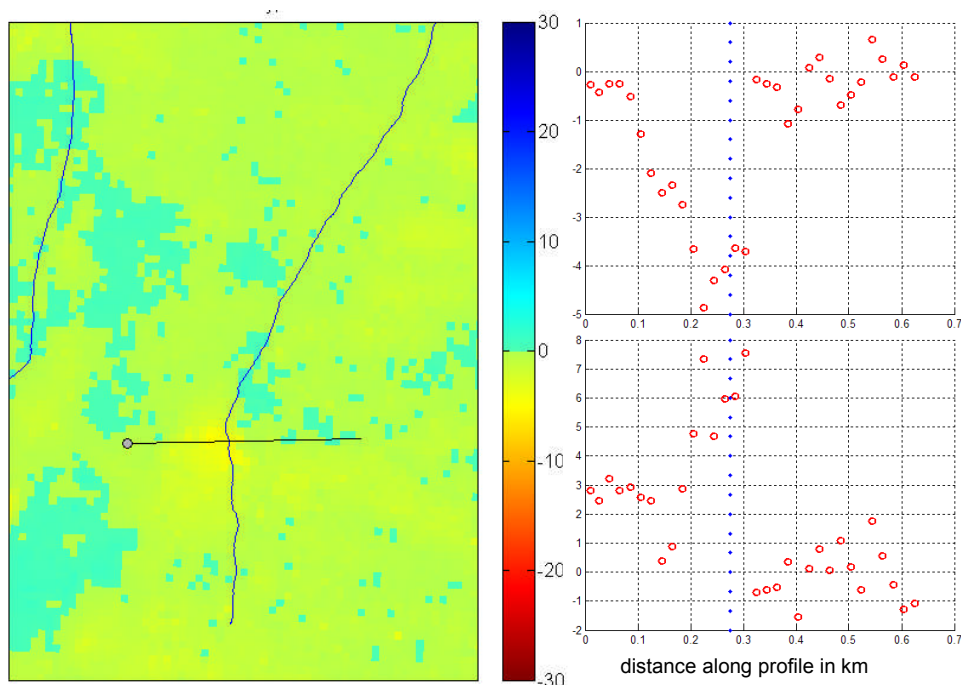
Figure 10. Example of a deformation signal across a fault (from Envisat). Left – map view showing color-coded vertical displacement rates in mm/year. Right – vertical (top) and west-east horizontal (bottom) deformation rates along profile. Vertical blue dotted line marks location where profile crosses the fault.

study area. Some of these patterns are seen in Figs. 2b-2d, and especially in Fig. 3.

It is of great interest to compare the InSAR results with other geophysical data, including the seismic velocities extracted from the seismic reflection lines in this project, gravity data, and temperature measurements. In particular, preliminary comparison with Bouguer gravity anomaly data, and especially the first vertical derivative, indicated a remarkable correspondence between the two sets of data. However, this observation is still not well understood and we continue looking into it, so findings will be discussed in future publications.

Conclusions

Satellite radar interferometry was used to detect and measure surface deformation in the San Emidio geothermal field. Uniquely rich results were obtained, which we continue to examine. Three satellite datasets were used between 1992 and 2010, thus providing an extended view of deformation in the area over time. The availability of data from two different orbital geometries made it possible to decompose line-of-sight deformation into vertical and horizontal movements. We demonstrated that deformation patterns in the area are affected by a combination of factors, such as geothermal production and injection, varying drought conditions, presence of fault traces and related hydrological control, and seasonal effects. The results demonstrate the value of this approach in obtaining unprecedentedly detailed information on surface deformation.

References

Eneva M., 2010. "Detection of surface deformation at mining and geothermal sites using satellite radar interferometry (InSAR)." In *Proceed. 44th U.S. Rock Mechanics Symposium and 5th U.S.-Canada Rock Mechanics Symposium, Salt Lake City, June 27-30, 2010.*

Eneva M., and D. Adams, 2010. "Modeling of surface deformation from satellite radar interferometry in the Salton Sea geothermal field, California." *Geothermal Resources Council Transactions* v. 34, p. 527-534.

Eneva M., G. Falorni, D. Adams, J. Allievi, and F. Novali, 2009. "Application of satellite interferometry to the detection of surface deformation in the Salton Sea geothermal field, California." *Geothermal Resources Council Transactions*, v. 33, p. 315-319.

Falorni G., J. Morgan, and M. Eneva, 2011. "Advanced InSAR techniques for geothermal exploration and production." *Geothermal Resources Council Transactions*, v. 35 (this issue).

Ferretti A., C. Prati, and F. Rocca, 2000. "Nonlinear subsidence rate estimation using permanent scatterers in differential SAR Interferometry." *IEEE Trans. Geosc. Rem. Sensing*, v. 38, p. 2202-2212.

Ferretti A., G. Savio, R. Barzaghi, A. Borghi, S. Musazzi, F. Novali, C. Prati, and F. Rocca, 2007. "Submillimeter accuracy of InSAR time series: Experimental validation." *IEEE Trans. Geosci. Rem. Sensing*, v. 45, p. 1142-1153.

Ferretti A., A. Fumagalli, F. Novali, C. Prati, F. Rocca, and A. Rucci, 2011. "A new algorithm for processing interferometric data-stacks: SqueeSAR." *IEEE Trans. Geosc. Rem. Sensing* (in press).

Moore J.N., 1979. "Geology map of the San Emidio geothermal area." U.S. DOE: Geothermal Energy, 78-1701.b.1.2.2, 8 p.

Oppliger G., L. Shevenell, and M. Coolbaugh, 2008. "Preliminary site assessment of the Redfield Campus, Reno, NV, USA." *Geothermal Research Council Transactions*, v. 32, p. 163-168.

Rhodes G.T., J.E. Faulds, and W. Teplow, 2010. "Structural controls of the San Emidio desert geothermal field, northwestern Nevada." *Geothermal Resources Council Transactions*, v. 34, p. 819-822.

Wicks C., W. Tatcher, F. Monastero, and M. Hasting, 2001. "Steady-state deformation of the Coso Range, east-central California, inferred from satellite radar interferometry." *J. Geophys. Res.*, v. 106, p. 13,769-13,780.

Wood J.D., 1990. "Geology of the Wind Mountain gold deposit, Washoe County, Nevada." In *Proceedings: Geology and Ore Deposits of the Great Basin*, eds. G.L. Raines, R.E. Lisle, R.W. Schafer, and W.H. Wilkinson, Geological Society of Nevada, p. 1051-1061.